Journal of Sound and Vibration (1998) **214**(3), 469–496
Article No. sv971575

ON THE VIBRATION FIELD CORRELATION OF RANDOMLY EXCITED FLAT PLATE STRUCTURES, II: EXPERIMENTAL VERIFICATION

M. W. Bonilha† and F. J. Fahy

Institute of Sound and Vibration Research, University of Southampton, Highfield, Southampton, SO17 1BJ, England

(*Received* 6 *May* 1997)

The results of an experimental investigation of vibration field spatial correlation carried out on two flat plate structures and on a car body shell are presented herein. The main purpose of this investigation was to assess the validity of the theoretical spatial correlation model presented in part I of this work [1]. Measurements of vibration acceleration were used as a means of estimating the frequency averaged spatial correlation coefficient of these structures under random excitation. It is observed that for cases of low modal overlap ($M < 1$) the analytical results are valid as a frequency average estimate in bands in which at least eight to ten modes are excited at resonance. For cases of high modal overlap ($M \gg 1$) the analytical results can be used as a narrow band estimate of the spatial correlation. Corrections proposed to account for the effects of mechanical excitation, presence of stiffeners and curvature are shown to be valid.

1. INTRODUCTION

An approximate representation of the spatial properties of the vibration field set up on a flat plate under random excitation was presented in part I of this work [1]. It was shown that such a model should be valid for the case of modally dense, lightly damped plates under spatially uncorrelated or point random excitation. The validity of such assumption is here tested by comparing theoretical spatial correlation coefficient results with experimental results obtained on two flat plate structures and on a car body shell.

Stearn [2] has shown that a close approximation to a diffuse bending wave field can be set up in a plate when more than ten modes are simultaneously excited. This was experimentally verified by comparing the spatial correlation coefficient for an ideal diffuse bending wave field to experimental results of spatial correlation obtained from acceleration measurements on a flat plate. In real, bounded flat plates, an approximation to this form of spatial correlation coefficient was experimentally observed in regions far from the edges and far from the excitation points.

Measurements of vibration field correlation were employed by Bonilha and Fahy [3] to assess the diffuseness of a car body shell. It was shown that in a non-uniform complicated structure, such as a fully trimmed roof composed of a doubly-curved shallow shell and reinforcing ribs with clamped edges, a near-perfect diffuse wave field can be set up only when an extremely large number of modes are simultaneously excited in a frequency band. The conclusions from references [2] and [3] indicate that the spatial correlation coefficient result for a diffuse bending wave field is not a good approximation for the representation

---

†Now at United Technologies Research Center, 411 Silver Lane, East Hartford, CT 06108, U.S.A.

0022–460X/98/280469 + 28 $30.00/0

of the spatial properties of randomly excited modally dense complicated structures close to the edges or perturbations.

It is well known that a diffuse sound field may be approximated in practice in the central region of a reverberant enclosure, at least half a wavelength away from any boundary, at frequencies above the Schroeder cut-off frequency, in cases of pure tone excitation [4]. When the excitation is of random nature, the diffuse sound field approximation may be achieved in finite frequency bands below the Schroeder cut-off frequency.

Close to the boundaries or any reflecting surface large compared to the wavelength, a sound field departs considerably from the diffuse state [5, 6]. The incident and reflected (or scattered) wave components superimpose either constructively or destructively, giving rise to interference patterns that are created by the reduction of the number of waves with uncorrelated random phase which contribute to the total pressure at a field point near the edges. In other words, waves within the incident and reflected sets may be uncorrelated with each other, but individual waves of the incident set are correlated with the corresponding waves of the reflected (or scattered) set. As a result of this interference, the sound energy is not uniformly distributed over the entire volume of a reverberant sound field. An analogous explanation applies to justify the departure of the diffuse bending wave field case near boundaries of reverberant bending wave fields.

The results of the work presented in reference [3] motivated the development of the theoretical representation presented in part I of this work [1] and an experimental procedure similar to the one employed in reference [3] was then applied to a number of flat plate structures. The flat plate structures of which the measured forms of spatial correlation are presented herein are (i) a 3·5 mm thick rectangular steel plate with a steel bar attached and clamped along the four edges (Figure 1) and (ii) a rectangular aluminium plate with free edges hung by two thin wires from a frame. Results for other structures are presented in reference [7].

These experimental results are compared with estimates of vibration field spatial correlation based on the theory presented in part I of this work [1]. In addition, results from a similar experimental investigation carried on a car body shell [3] are compared with the theoretical estimates. Modal density and structural loss factors estimates were also made as means of assessing their modal overlap factors and the number of modes resonating in each frequency band.

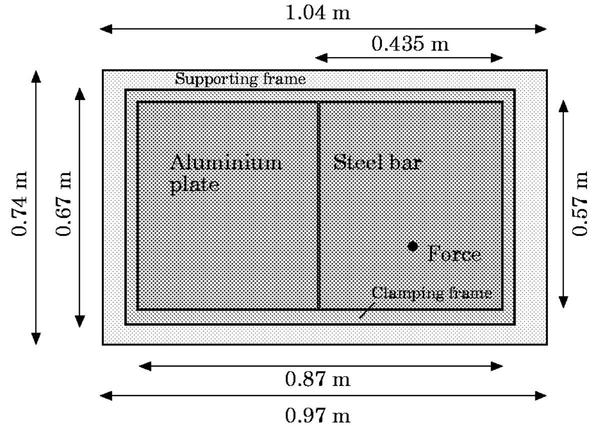

Figure 1. Sketch of rig with clamped plate and steel bar.

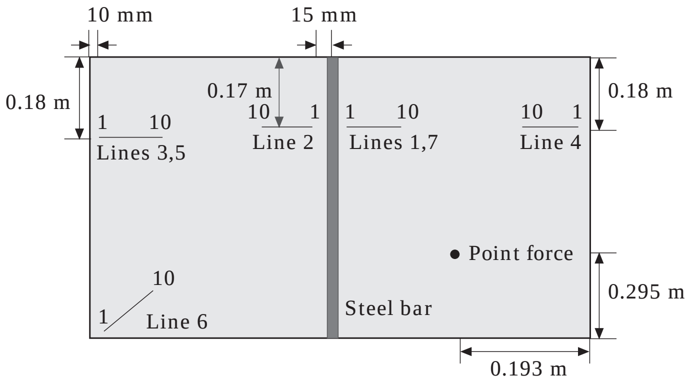

Figure 2. Position of measurement lines and excitation point on clamped plate with stiffener.

2. EXPERIMENTAL PROCEDURE

The applied experimental procedure was similar for all flat plates. Each plate was mechanically or acoustically excited by broad band random signals. These sources produced sufficient vibrational response to guarantee a good signal-to-noise ratio; the response levels were, in average, 30 dB higher than the background noise level. Two accelerometers (Bruel & Kjaer Type 4374) were placed along various tracks on the plate surface. In each set of measurements one accelerometer was held at one extreme of the track (marked 1 in Figures 2, 16 and 22) and the other was displaced from it along the line at equally spaced points.

The acceleration signals were acquired using a ZONIC + AND 3524 Dual Channel FFT Analyzer and transferred to a PC-compatible microcomputer. The frequency averaged spatial correlation coefficient ($\gamma_{12}(\mathbf{x}_1, \mathbf{x}_2, f_c)$) between the two acceleration signals was then estimated using the following equation,

$$\gamma_{12}(\mathbf{x}_1, \mathbf{x}_2, f_c) = \int_{f_1}^{f_2} \mathrm{Re}\,[G_{12}(\mathbf{x}_1, \mathbf{x}_2, f)]\,\mathrm{d}f \Bigg/ \left[\int_{f_1}^{f_2} G_1(f)\,\mathrm{d}f\right]^{1/2} \left[\int_{f_1}^{f_2} G_2(f)\,\mathrm{d}f\right]^{1/2}. \qquad (1)$$

For this purpose, the cross-power spectrum $G_{12}(\mathbf{x}_1, \mathbf{x}_2, f)$ and auto-power spectra $G_1(f)$ and $G_2(f)$ of acceleration in each pair of points were acquired in the frequency range 0–5000 Hz. These estimates were integrated in 1/3 octave bands and in bands of constant width. The frequency separation of these spectra was 3·125 Hz (1600 lines) for all lines. Finally, the frequency averaged estimates were plotted as a function of the non-dimensional distance kr, where k is the bending wavenumber calculated at the band centre frequency and r is the distance in metres between each pair of points.

A large accelerometer can considerably load thin plates such as those here investigated. As a result lightweight accelerometers (B&K 4374, mass 0·6 grams) were chosen for this investigation and it was estimated that they only affected the present results for frequencies above 3000 Hz for the car roof (thickness = 0·8 mm). For the other plates the mass load of the accelerometer was negligible. In addition, it is important to mention that as the correlation coefficient is a normalised quantity this mass load effect will be cancelled when the experimental results are combined using equation (1).

One-third octave bands were chosen for the analysis because, in such bands, the bending wavenumber of each resonant mode does not vary more than 6% from the assumed mean value of the bending wavenumber (k_b) corresponding to the band centre frequency. This can be explained by the fact that the bending wavenumber is proportional to the square

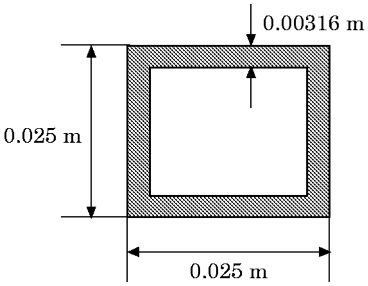

Figure 3. Cross-section of steel bar used as a stiffener.

root of the associated frequency. So, if the square root of upper or lower frequency limits of one-third octave bands are divided by the square root of the band centre frequency the result is close to 6%.

The repeatability of the measurements were verified by estimating the spatial correlation coefficient for the same pair of points ten times. In this exercise, before each set of acceleration signals were acquired, both accelerometers were removed and re-fixed to the plate as a way of simulating a real laboratory situation. The largest normalised standard deviation (σ/m) of the estimated correlation coefficient was 0·1. Expressions for the errors associated with the spatial correlation coefficient estimation are used to estimate the variance and the confidence limits of the measurements, as described in Appendix A.

3. RECTANGULAR STIFFENED PLATE WITH FOUR CLAMPED EDGES

3.1. DESCRIPTION OF THE APPARATUS

The flat plate was of 3·53 mm thick aluminium. It was (weakly) clamped by hard rubber strips along the edges set into a wooden frame which was placed on a rigid wooden table (Figure 1). The exposed dimensions of the plate were 0·87 m × 0·57 m and it was divided, along its larger dimension, into two equal areas by a hollow steel bar having a cross-sectional area of (25 × 25) mm^2 and thickness of 3·16 mm (Figure 3). The steel bar was fixed to the plate by five light screws. This permitted the easy removal of the steel bar, enabling a comparison to be made of the vibration characteristics of the plate with and without the stiffener. The first three natural frequencies of transverse, longitudinal and torsional vibration of this bar are listed in Table 1: those frequencies were computed following the expressions presented by Blevins [8]. As shown in this table, the steel bar does not have many resonance frequencies in the frequency band of analysis.

Typical wavelengths for the plate were: 0·415 m at 200 Hz, 0·24 m at 600 Hz, 0·186 m at 1000 Hz and 0·131 Hz at 2000 Hz. Point excitation by an electrodynamic shaker (Ling Dynamic V101) was used to vibrate the plate. The excitation signal employed was

Table 1

Natural frequencies of vibration of the steel bar

order of natural frequency	transverse vibration (Hz)	longitudinal vibration (Hz)	torsional vibration (Hz)
1	500·6	4489·8	2387·2
2	1379·0	8979·6	4774·4
3	2705·6	13469·0	7161·6

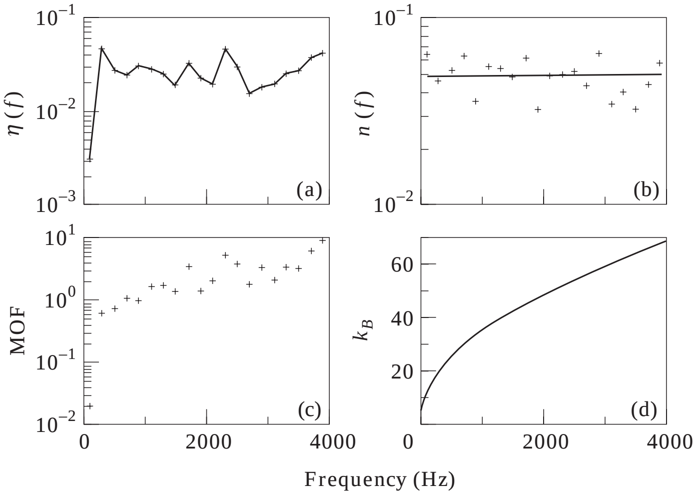

Figure 4. Loss factor, modal density and modal overlap factor experimental estimates on clamped plate (0·87 m × 0·57 m × 3·5 mm) without stiffener. Frequency bands of 200 Hz bandwidth. (a) Loss factor; (b) modal density; (c) modal overlap factor; (d) dispersion curve. Key for (b): + +, experimental; ——, theoretical.

broadband random from 0–5000 Hz. The point marked 'Point force' in Figure 2 indicates the position on which the force was applied. The vibrational response obtained was sufficiently high to guarantee a good signal-to-noise ratio.

The experimental procedure employed was that described in section 2 and the tracks used are illustrated in Figure 2. Lines 3 and 5, and lines 1 and 7 were coincident; however results for lines 5 and 7 were carried out for the plate without the stiffener. The spacing between the ten points used on each line was 1 cm.

The theoretical results used for the comparison with the experimental ones are derived in part I of this work [1]: equation (30) with the dynamic edge parameters given by expressions (B4) for a clamped edge and by expressions (B10), (B11) and (B12) for a spring supported edge (the steel bar dynamic characteristics defined the spring rotational, translational and coupling stiffnesses, as shown in Appendix B of part I [1]).

The loss factor and modal density of this plate were estimated via measurement of point mobility and power injection following the procedure suggested by Clarkson as described in references [9, 10]. As only an approximate estimate of these parameters was required, the point mobility was obtained in just one point. Ideally, at least three measurement points should be used in order to obtain a spatially-averaged estimate. The shaker was fed with a broadband random signal from the FFT analyser and the accelerometer was placed on the opposite face of the plate in line with the shaker contact point. Modal density estimates obtained following this procedure were similar to theoretical predictions (Figure 4).

The loss factor, modal density and modal overlap factor results obtained for the plate with and without stiffeners are shown in Figures 4 and 5. The results presented in these figures are for constant bands of 200 Hz and the modal overlap factor was estimated from the relation $M = \eta(f_c)n(f_c)f_c$ [11], where f_c is the band centre frequency, $n(f_c)$ is the modal density and $\eta(f_c)$ is the loss factor. Typical estimated point mobilities for both stiffened and non-stiffened cases are presented in Figures 6 and 7. In the loss factor estimation, only one excitation point and ten vibration velocity measurement points were employed. Nevertheless, the loss factor results obtained were similar to the ones reported by Mohammed [11] for the same plate and test apparatus.

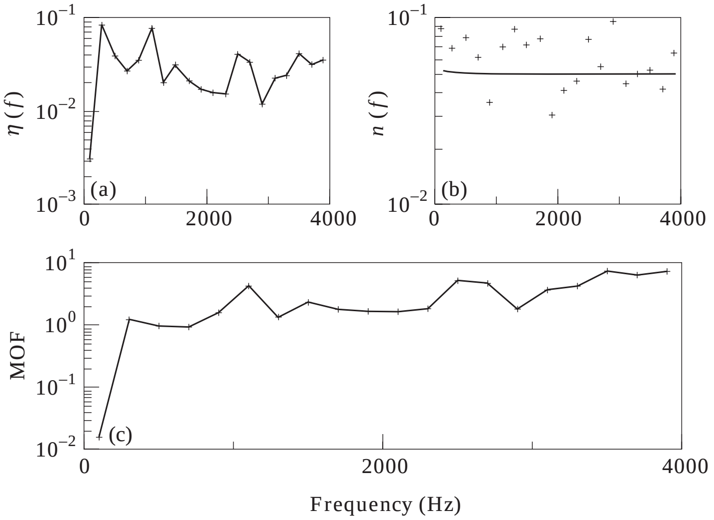

Figure 5. Experimental results of loss factor, modal density and modal overlap factor for clamped plate with stiffener. Constant bands of 200 Hz. (a) Loss factor; (b) modal density; (c) modal overlap factor. Key; +—+, whole panel; + +, experimental; ——, theoretical.

The results presented in Figure 5 are for the plate with the stiffener excited at only one point. As expected, the loss factor for the plate with the stiffener (Figure 5) is slightly higher than that for the plate without the stiffener (Figure 4). The stiffened plate theoretical modal density employed in the comparison was calculated as the sum of the modal density of a flat plate with flexural vibration and of a uniform beam in flexural vibration (equation (6.24), reference [9]).

3.2. RESULTS FOR THE PLATE WITHOUT STIFFENER

The results for the spatial correlation coefficient for the plate without a stiffener are presented in this section. Results from lines 5, 6 and 7 were used in this part of the work.

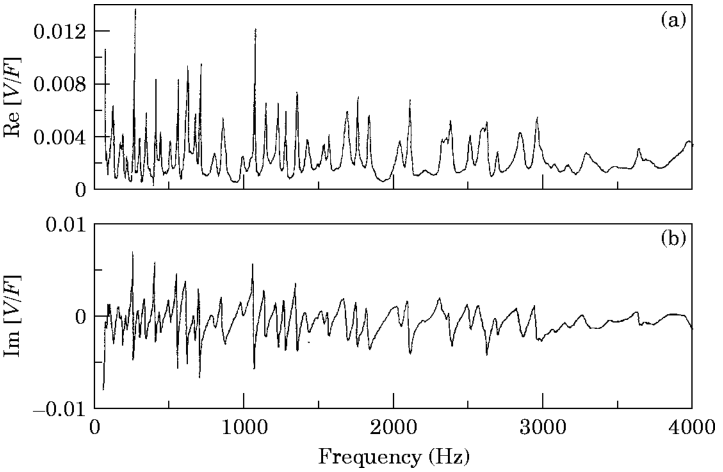

Figure 6. Real and imaginary parts of point mobility for clamped plate without stiffener: (a) real; (b) imaginary.

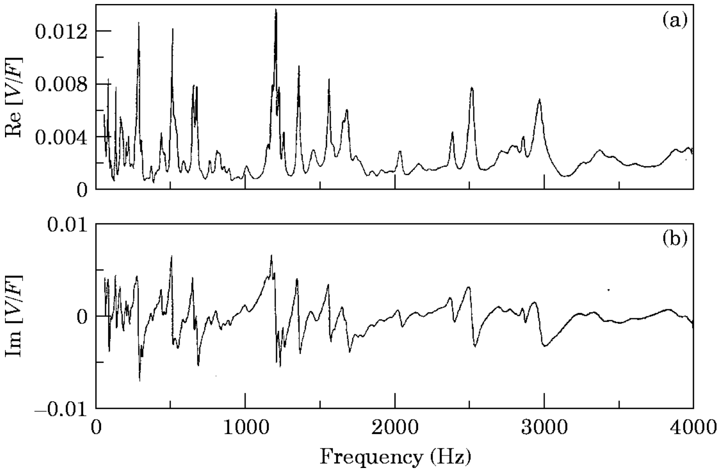

Figure 7. Real and imaginary parts of point mobility for clamped plate with stiffener: (a) real; (b) imaginary.

A common characteristic of the results from lines 5, 6 and 7 was that, above the 1000 Hz one-third octave band, all experimental results approached the theoretical results (given by equation (30) combined with parameters (B4) of reference [1]). Figures 8 and 9 were included in order to illustrate this observation. As a matter of fact, it is clearly shown in Figure 9 that in each one-third octave band above 1250 Hz, the theoretical results on line B approach the experimental results. Reasons for this are two-fold: first, the number of modes that have resonance frequencies inside the 1250 Hz one-third octave band was estimated to be 14, which is higher (even if one assumes that 25% of the modes are not excited due to shaker position) than the figure of eight modes suggested in the reference [1] and ten as suggested by Stearn [2]. Second, from Figure 4 it is observed that above 1000 Hz the modal overlap factor is greater than unity.

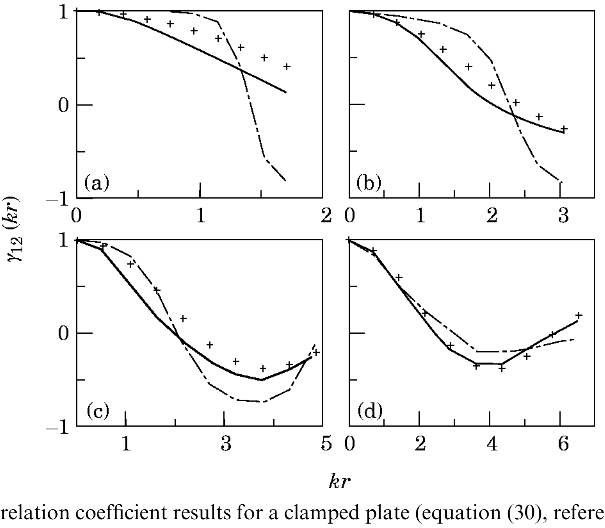

Figure 8. Spatial correlation coefficient results for a clamped plate (equation (30), reference [1]) compared with experimental results due to point mechanical excitation. Line 7, one-third octave bands. Key: ——, theory (equation (30), reference [1]); –·–·–, experimental results; + + diffuse bending wave field (equation (21), reference [1]). (a) 315 Hz; (b) 1000 Hz; (c) 2500 Hz; (d) 4000 Hz.

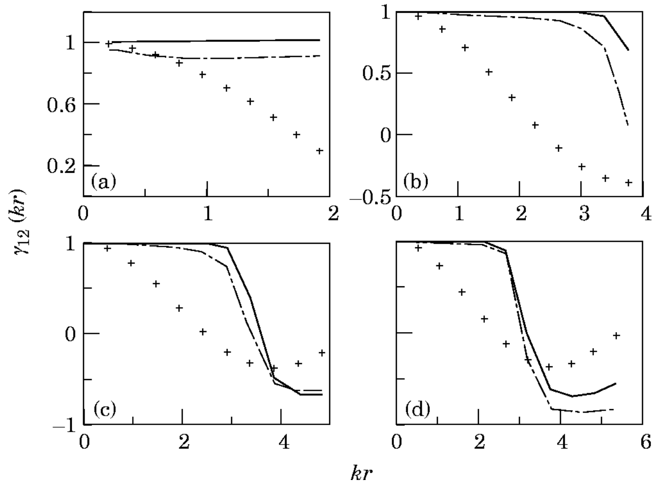

Figure 9. Spatial correlation coefficient results for a clamped plate (equation (30), reference [1]) compared with experimental results due to point mechanical excitation. Line 6, one-third octave bands. Key: ——, theory (equation (30), reference [1]); –·–·–, experimental results; + + diffuse bending wave field (equation (21), reference [1]). (a) 315 Hz; (b) 1250 Hz; (c) 2000 Hz; (d) 2500 Hz.

It was confirmed by modal summation results (reference [1]) that at points removed from the edges (at least one wavelength from the edges), simply supported plate correlation coefficient results converge to those of a diffuse bending wave field. The same verification was carried out for points situated along line 7 of the clamped plate as, for most frequency bands, these points were outside the one-wavelength-from-the-edges region. It is clearly shown in Figure 8 that, above 1000 Hz, the diffuse bending wave field (equation (21) of reference [1]) and the clamped plate theoretical results are very similar and they both approach the experimental results. This was expected because the estimated wavelength at 2000 Hz was 0·131 m and thus, only the inner solution of Bolotin's edge effect method contributes to the analytical clamped plate result. Similar results were obtained for plates with free edges (section 4).

On the other hand, the points situated along line 6 are situated inside the one-wavelength-from-the-edges region for most frequency bands analysed. As shown in Figure 9, the diffuse bending wave field results for points along this line depart considerably from experimental and theoretical (clamped plate) spatial correlation coefficient results. This confirms what was observed in part I of this work [1] for the case of points near the edges on simply-supported flat plates, showing the effect of the edges in correlating the vibration field in regions one wavelength from the edges. In addition, in view of the good agreement between theoretical (clamped plate) and experimental results, it also shows the importance of including the outer solution of Bolotin's dynamic edge effect method in the theoretical derivation of results for points close to clamped edges. Similar results were also observed for points close to free edges as shown in section 4.

As a means of checking the combined role of number of modes in the band and modal overlap factor in the applicability of the present approach on a practical situation, the results obtained on lines 6 and 7 were averaged in bands of 10 Hz, 40 Hz, 100 Hz and 400 Hz in regions of low and high modal overlap. Some of such results obtained at line 6 are shown in Figure 10. On the one hand, it is observed that for regions in which the modal overlap factor is higher than unity, the frequency averaged correlation coefficients are similar to the theoretical ones, even in a narrow band of only 10 Hz: the correlation characteristics are rather insensitive to frequency bandwidth. On the other hand, for frequencies regions in which the modal overlap factor is lower than unity, the frequency averaged correlation coefficients are extremely dependent on the width of the frequency band. Results from other frequency bands show similar behaviour.

Stearn [12] reported that the degree of modal overlap does not influence spatial correlation coefficient results. This is a result that is not corroborated by the present work. With the purpose of double-checking the present observations, the frequency average was performed in bands of 10 Hz and 600 Hz for eight frequency bands whose centre frequencies were equally spaced. One group of frequencies was situated in a region of modal overlap factor lower than unity and the other group of frequencies was placed in a region of modal overlap factor higher than unity. A separation of 20 Hz was chosen for the centre frequencies to assure that the points from the line spectra used in the averaging process for the 10 Hz band were different in each consecutive band.

Results for the frequency region with low modal overlap are presented in Figure 11 for points placed along line 7. The modal overlap factor in this frequency region was estimated to be around 0·6 as shown in Figure 4. It is verified in Figure 11 that the 600 Hz result is always close to the theoretical estimate but the 10 Hz result varies considerably between each adjacent band. The 10 Hz frequency averaged results clearly exhibit modal behaviour, indicating that the modes in this frequency region are not overlapping (see Figures 6 and 12). If one examines a typical frequency response function of this plate (Figure 12), three clear resonance frequencies are observed in this frequency region: the first at around 330 Hz, the second at 400 Hz and the third at 440 Hz. This explains why the 10 Hz frequency averaged results at centre frequencies 320 Hz and 340 Hz are so similar and at the same time why they are so different from results at centre frequencies 400 Hz or 460 Hz.

The modal overlap factor is a measure of the ratio between average modal bandwidth ($\eta\omega$) and average separation between resonance frequencies ($\delta\omega = 1/n(\omega)$), where $n(\omega)$ is the modal density. Modal half-power bandwidth is defined as the difference between the frequencies at which the mean square modal response is half its maximum value (3 dB down). A modal overlap factor equal to or higher than unity indicates that at least three natural modes contribute significantly to the system response in a single frequency. A high

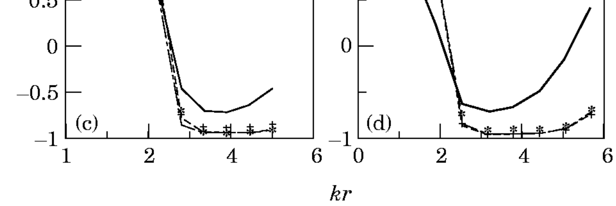

Figure 10. Frequency averaged spatial correlation coefficients along line 6. Experimental results due to point mechanical excitation averaged in bands of different widths: Key: ——, theory (equation (30), reference [1]); –·–·–, 10 Hz band; + + + 40 Hz band; - - - -, 100 Hz band; ***, 400 Hz band. (a) 300 Hz; (b) 2300 Hz; (c) 2700 Hz; (d) 3500 Hz.

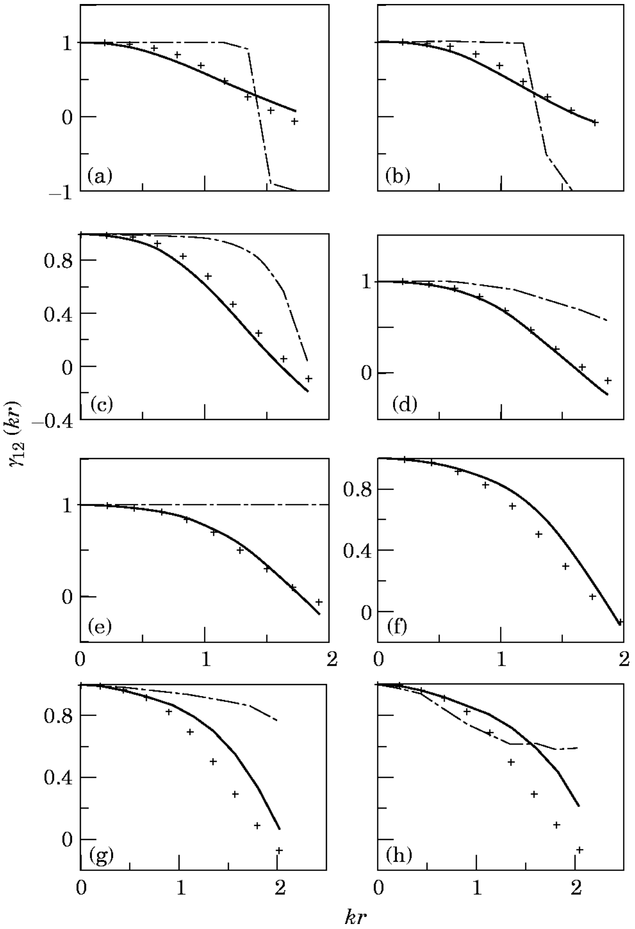

Figure 11. Frequency averaged spatial correlation coefficients along line 7 for non-stiffened plate. Experimental results due to point mechanical excitation averaged in bands of different widths with modal overlap factor $\cong 0{\cdot}6$. Key: ——, theory (equation (30), reference [1]); —·—·—, 10 Hz band; + + + 600 Hz band. (a) 320 Hz; (b) 340 Hz; (c) 360 Hz; (d) 380 Hz; (e) 400 Hz; (f) 420 Hz; (g) 440 Hz; (h) 460 Hz.

modal overlap also implies a smooth frequency response function in which individual resonance frequency peaks can not be distinguished. Such smooth behaviour are exemplified by the point mobility results above 3000 Hz presented in Figures 6 and 12.

Results for a frequency region in which the modal overlap factor is higher than unity are presented in Figure 13 for points placed along line 6. The modal overlap factor in this frequency region was estimated to be around 2·5. It is observed that, for frequency averages carried out in 10 Hz bandwidths, the results did not vary strongly between each adjacent band. Moreover, these results generally lie close to those averaged over 600 Hz bands (with the clear exception of centre frequency 3020 Hz) and as consequence are not far from the theoretical estimates. The small difference between the theoretical and the experimental results observed in Figures 10 and 13 are assumed to be related to the boundary conditions which are not perfectly clamped. It is not expected that such agreement would be improved if more points were used in the digital discretization of the response signals for the 10 Hz frequency-averaged results.

3.3. RESULTS FOR THE PLATE WITH A STEEL BAR (STIFFENER) ATTACHED

This section presents the experimental results of the spatial correlation coefficient on the clamped plate with the steel bar attached. In this investigation, only one side of the panel was directly excited (as illustrated in Figure 2). The influence of the steel bar on the plate vibrational field is illustrated by comparing Figures 6 and 7. The frequency response function has changed and is now much more complex than the one for the unstiffened plate. As a matter of convenience the stiffened plate was represented by two separate plate subsystems. In this model the steel bar acts as a coupling element between the two sides of the plate, reflecting and transmitting the incident energy.

Some of the results obtained for points placed along lines 3, 4 and 5 are presented in Figure 14. The points used on these lines had similar distances to the nearest two edges and thus the theoretical model gave the same result for the three lines. As already explained, lines 3 and 5 were coincident, though line 5 indicates measurements made on the plate without the stiffener and line 3 on the plate with the stiffener. Results for line 4 were for the panel with the steel bar attached. Above 1000 Hz, results for all three lines were similar (e.g., 1250 Hz results presented in Figure 14) while below 1000 Hz those results were quite different (e.g., 630 Hz results presented in Figure 14). As observed on the plate without the stiffener (section 3.2), the frequency averaged experimental results approached the theoretical ones in one-third octave bands above 1250 Hz. This is a clear indication that, as predicted by the present theoretical model, the influence of both clamped edges is dominant on the region in which lines 3 and 4 are situated. Moreover, this also shows that a perturbation placed outside a region one wavelength far from the measurement points will not affect the frequency averaged spatial correlation coefficient associated with these points. However, for points situated in a region less than one wavelength far from the perturbation (steel bar) the situation is quite different.

As presented in Figure 15, experimental results of the spatial correlation coefficient obtained on the right (line 1) and left (line 2) sides of the steel bar were dissimilar. In order to represent this situation the theoretical spatial correlation coefficients were estimated on the basis of the two subsystems model. On the side in which the panel was directly excited,

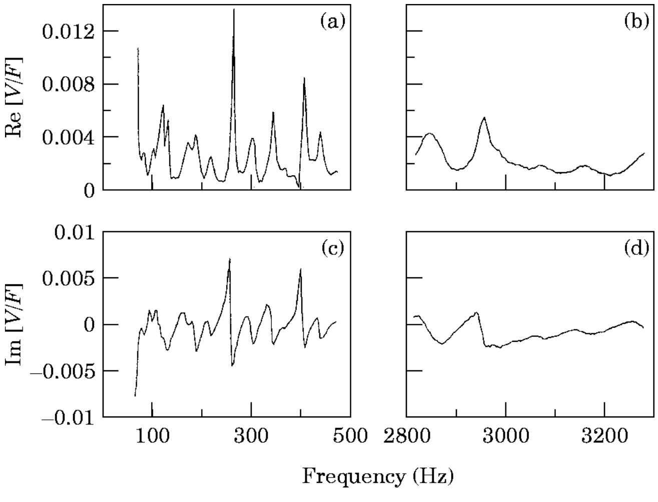

Figure 12. Frequency response functions (velocity/force) on clamped plate without stiffeners 0–500 Hz and from 2800–3300 Hz. Plotted as real and imaginary parts. Point mobilities: (a)–(c) 0–500 Hz; (b)–(d) 2800–3300 Hz.

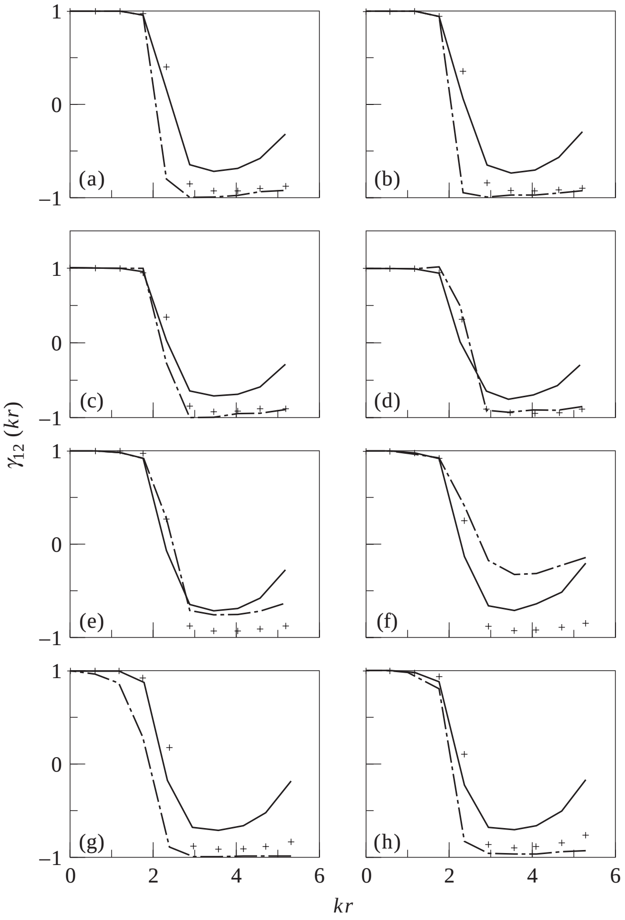

Figure 13. Frequency averaged spatial correlation coefficients along line 6 for non-stiffened plate. Experimental results due to point mechanical excitation averaged in bands of different widths with modal overlap factor $\cong 2{\cdot}5$. Key: ——, theory (equation (30), reference [1]); —·—·—, 10 Hz band; + + + 600 Hz band. (a) 2920 Hz; (b) 2940 Hz; (c) 2960 Hz; (d) 2980 Hz; (e) 3000 Hz; (f) 3020 Hz; (g) 3040 Hz; (h) 3060 Hz.

the correlation coefficients were calculated using the reflection and evanescent (reflection side) field component coefficients (Appendix B). On the indirectly excited side the transmission and evanescent (transmission side) field component coefficients (Appendix B) were used for points approaching the steel bar. These wave coefficients were transformed into Bolotin's dynamic edge effect method parameters (reference [1]) using the equivalence equations presented in Appendix B. Near the other boundaries, parameters for a clamped edge were used.

In the region in which line 1 was situated the reflected and evanescent reflected field components were dominant and the theoretical model employed was able to predict the correlation coefficient with reasonable success on one-third octave bands above 1000 Hz. On the other hand, transmitted and transmitted evanescent field components were more important in the region in which line 2 was placed. Again, the theoretical model was able to predict such results with reasonable success. Below 1000 Hz, no agreement between the theoretical and experimental results was achieved.

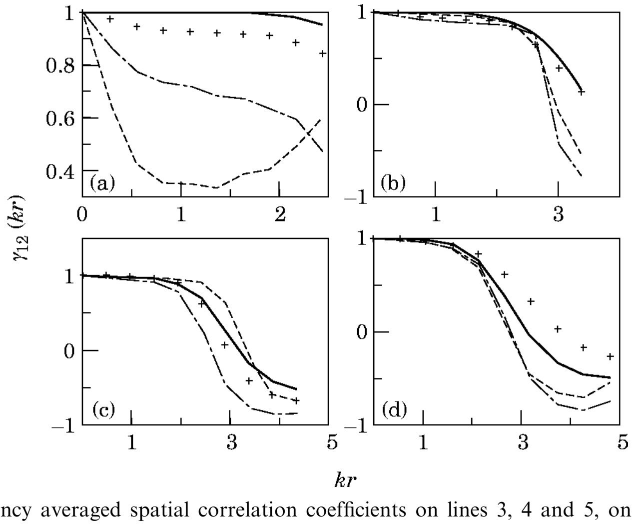

Figure 14. Frequency averaged spatial correlation coefficients on lines 3, 4 and 5, one-third octave bands. Experimental results due to point mechanical excitation. Key: ——, theory (equation (30), reference [1]); —·—·—, line 3; + + + line 4; - - - - line 5. (a) 630 Hz; (b) 1250 Hz; (c) 2000 Hz; (d) 2500 Hz.

4. RECTANGULAR FLAT PLATE WITH FOUR FREE EDGES

The aim of this part of the investigation was to check the theoretical results for boundary conditions other than simply supported, clamped or spring supported. With the addition of the free boundary condition all boundary conditions encountered in practice could be covered. A free edge boundary condition is not directly relevant to practical studies of acoustic radiation; however it can give a lower limit of sound pressure levels inside an enclosure that can be achieved by modifying the structure boundary conditions. This type of control has been discussed by Cheng and Nicolas [13].

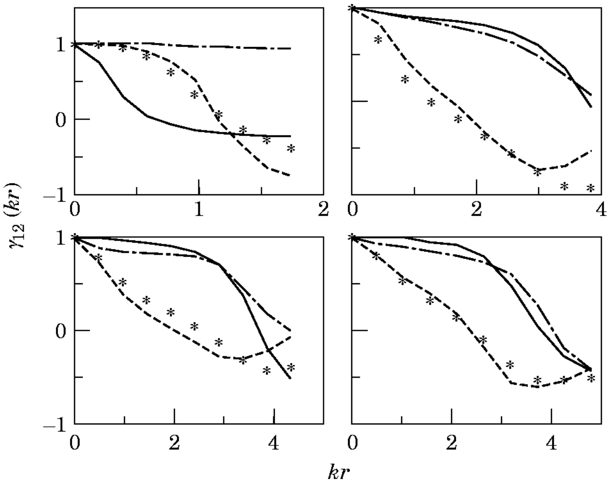

Figure 15. Frequency averaged spatial correlation coefficients on lines 1 and 2, one-third octave bands. Point mechanical excitation on side in which line 1 is placed. Line 1, key: ——, theory (equation (30), reference [1]); —·—·—, experimental. Line 2, key: ***, theory (equation (30), reference [1]); - - - -, experimental. (a) 315 Hz; (b) 1600 Hz; (c) 2000 Hz; (d) 2500 Hz.

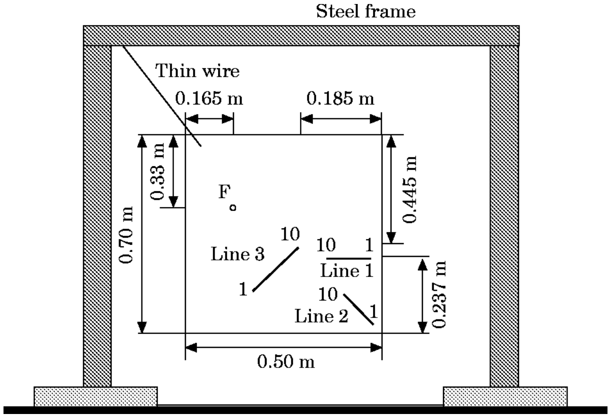

Figure 16. Sketch of experimental rig and lines used on free rectangular plate.

4.1. DESCRIPTION OF THE APPARATUS

A flat aluminium plate of 2 mm thickness suspended by two thin wires from a steel frame was another structure used in this experimental investigation. The plate was of rectangular geometry with sides of 0·50 m and 0·70 m length and it had free boundary conditions all along the edges. No damping material was placed on the plate. A sketch of the plate and rig used are shown in Figure 16. Typical bending wavelengths for this plate were: 0·442 m at 100 Hz, 0·167 m at 700 Hz, 0·14 m at 1000 Hz and 0·081 m at 3000 Hz. The plate was excited with broadband random excitation from 0–5000 Hz by an electrodynamic shaker (Ling Dynamic V101) at only one position (marked F on Figure 16).

The experimental procedure employed in this investigation is described in section 2. Acceleration signals were acquired in pair of points situated along lines 1, 2 and 3, as illustrated in Figure 16. The measurement points were placed along these lines in 1 cm steps. The first point of line 1 was placed just 5 mm from the edge while the first point of line 2 was situated 10 mm from the plate corner.

The theoretical results for the spatial correlation coefficient as described in part I [1] were compared to the experimental results presented herein. They were obtained from numerical integration of equation (30) of reference [1] with the parameters for free edges shown in equations (B5) to (B7) of reference [1].

In view of the low damping of this plate the modal overlap was low within the frequency range analysed. The estimated modal density for this plate was 0·056 modes/Hz and the average dissipation loss factor was assumed to be around 0·001 [10]. Thus, typical values of modal overlap factor were: 0·005 at 100 Hz, 0·03 at 600 Hz, 0·05 at 1000 Hz and 0·22 at 4000 Hz. An illustration of a typical frequency response function (point inertance at the excitation point) is presented in Figure 17 and it is observed that most of the resonance peaks do not overlap within 0–4000 Hz range. Therefore, the experimental results were only expected to agree with theoretical ones for frequency bands with width greater than 200 Hz, as more than ten modes are estimated to be excited in this bandwidth.

4.2. DISCUSSION OF RESULTS

Experimental results obtained on lines 1, 2 and 3 and that were averaged in one-third octave bands agreed with theoretical results above the 800 Hz one-third octave band. This is in accordance with the findings presented in section 3.2 as the bandwidth of the 800 Hz one-third octave band is 183 Hz and ten modes were predicted to be excited at this frequency band. In addition, good agreement was also observed for lines 1 and 2 on some frequency bands below 800 Hz.

In particular, results for line 2, as shown in Figure 18, agreed with the theory on all frequency bands analysed and the agreement was exceptionally good above, and including, 250 Hz. Such good agreement near the corner was rather surprising as the Bolotin's dynamic edge effect method parameters presented in Appendix B of reference [1] were derived assuming that only one edge is important to the edge solution and the other three edges do not affect this solution. This is a standard assumption of Bolotin's dynamic edge effect method [14] and it is the type of consideration normally associated with the derivation of reflection coefficients on flexural wave motion [15]. Nevertheless, the agreement observed on line 2 demonstrates that the frequency averaged spatial correlation model here presented is a valid approximation even near the corner of a structure.

All the 18 one-third octave bands analysed (80 Hz–4000 Hz) are included in Figure 18 in order to illustrate how experimental and theoretical results compare. As shown, there is a spread between good and bad agreement in different frequency bands. In general, in this work, when one suggests there is a good agreement between experimental and theoretical results it is because more than fifty percent of all bands in a frequency region present good matching between experimental and the theoretical results. Due to space limitations, it is not practicable to include all frequency bands analysed for each of the lines studied in the different plates used in the experimental investigation. As a result, only four bands are chosen for each line in order to illustrate the main points discussed.

A slight disagreement between theoretical and experimental results was observed at the one-third octave band centred on 4000 Hz, as shown in Figure 18. In this high frequency range, the theoretical results begin to depart from the experimental ones. This happens because the importance of the second order terms in the solution of integral (18) of reference [1] increase with the width of the integration strip. Therefore, the analytical approximation used for this integral is no longer strictly valid.

A selection of one-third octave band results obtained on lines 1 and 3 is presented in Figures 19 and 20. As already mentioned, reasonable agreement with the theory has been observed on some frequency bands below 800 Hz. This agreement was more pronounced for points approaching the edges (line 1) and the corners (line 2) even when less than 4 modes are estimated to be excited in one frequency band (e.g., 250 Hz one-third octave

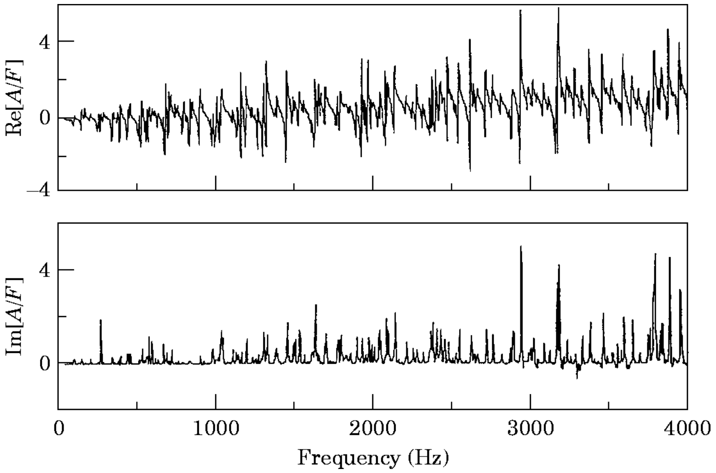

Figure 17. Frequency response function of aluminium plate with free edges. Point inertance: (a) real (b) imaginary.

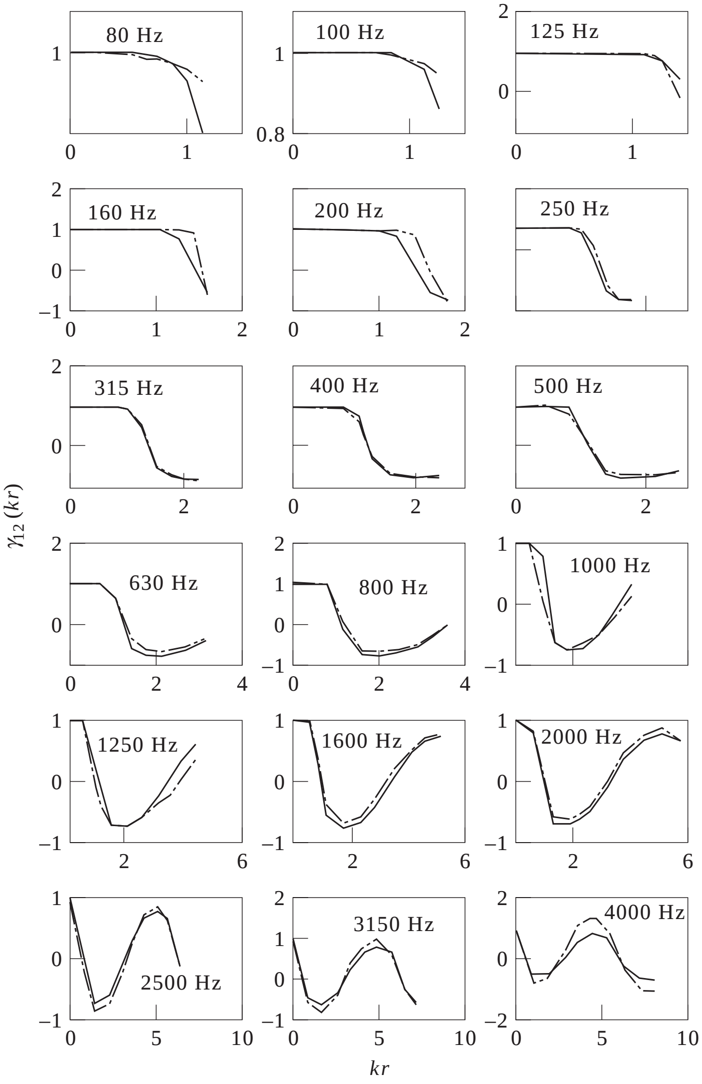

Figure 18. Frequency averaged spatial correlation coefficients along line 2 on free rectangular plate, one-third octave bands. Experimental results due to point mechanical excitation. Key: ——, theory (equation (30), reference [1]); —·—·—, experimental results.

band). This is probably due to the interference of the waves near the edges. On the other hand, for points far from the edges (in terms of wavelength) the suggestion (section 3 and reference [1, 2]) that eight to ten modes need to be excited in a frequency band for the validity of the present model is also applicable to the case of free edges.

Spatial correlation coefficients frequency averaged in narrow bands were not expected to agree with theoretical results due to the vibration field low modal overlap. This was confirmed by the computation of frequency averaged results in bands of varying width. The only exception were results on line 2 as most of the narrow band results (10 Hz and 40 Hz) were also similar to results in wider bands (100 Hz and 400 Hz). An example of this agreement on line 2 is presented in Figure 21 for bands with centre frequency 300 Hz. The strong interference near the corner appears to be the explanation for this agreement.

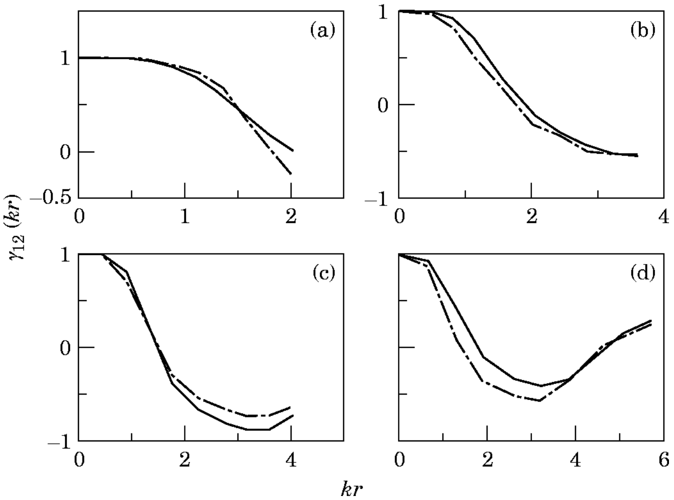

Figure 19. Frequency averaged spatial correlation coefficients along line 1 on free rectangular plate, one-third octave bands. Experimental results due to point mechanical excitation. Key: ——, theory (equation (30), reference [1]); —·—·—, experimental results. (a) 250 Hz; (b) 800 Hz; (c) 1000 Hz; (d) 2000 Hz.

On the other lines, only results that were frequency averaged in 400 Hz bandwidths approached the theoretical results.

5. ROOF AND WINDSCREEN OF A PASSENGER CAR

In references [3, 16] results of measurements of vibration field correlation carried out on different parts of a car body shell are reported. Such results indicate that even when a large number of modes are excited in a frequency band a diffuse field is not necessarily

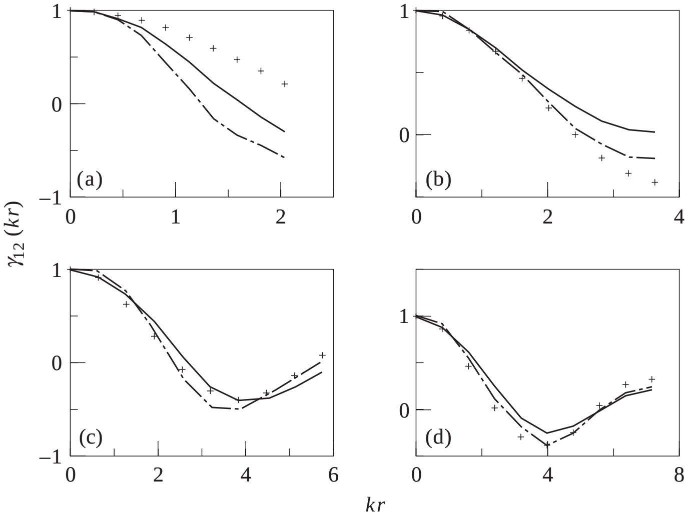

Figure 20. Frequency averaged spatial correlation coefficients along line 3 on free rectangular plate, one-third octave bands. Experimental results due to point mechanical excitation. Key: ——, theory (equation (30), reference [1]); —·—·—, experimental results; + + +, diffuse bending wave field result (equation (21), reference [1]). (a) 250 Hz; (b) 800 Hz; (c) 2000 Hz; (d) 3150 Hz.

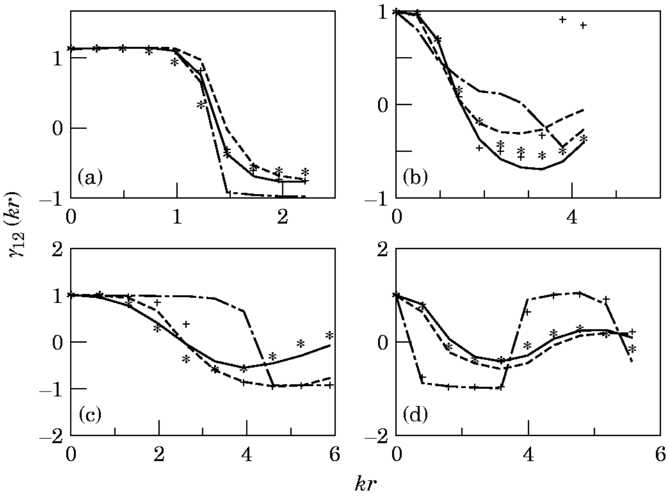

Figure 21. Frequency averaged spatial correlation coefficients along lines 1, 2, 3 on free rectangular plate. Experimental results due to point mechanical excitation averaged in bands of different widths. Key: ——, theory (equation (30), reference [1]); —·—, 10 Hz; + + +, 40 Hz; - - - -, 100 Hz; ***, 400 Hz. (a) line 2, 300 Hz; (b) line 1, 1100 Hz; (c) line 3, 2100 Hz; (d) line 1, 3100 Hz.

set up in a two-dimensional plane structure. In part, the results of that investigation motivated the development of the approach presented in part I of this work [1], as a means of representing vibration field correlation for different boundary conditions. Thus, in what follows, a comparison between some of those experimental results and the model suggested in part I [1] is presented.

5.1. EXPERIMENTAL PROCEDURE AND DESCRIPTION OF THE APPARATUS

Vibration field correlation measurements, identical to the ones reported in the previous sections, were made on the body of a Nissan Bluebird passenger car which was parked inside a laboratory room measuring 8 m × 5 m × 3 m. Three sources of random excitation were used (i) that of a reverberant sound field set up by acoustically exciting the laboratory room with white noise; (ii) that of a sound field set up by acoustically exciting the car interior with white noise; and (iii) that set up by mechanically exciting the car offside lateral pillar.

Two lightweight accelerometers (Bruel & Kjaer 4374) were placed along different lines on certain parts of the car body. Results for four lines on the roof (shown in Figure 22) and two on the windscreen (also shown in Figure 22) are here included. Results at other lines along the car body were also obtained and presented in reference [16]. In each set of measurements one accelerometer was held at the beginning of the line (marked 1 in Figure 22) and the other displaced from it along the line at eight equally spaced points. The spacing varied with the frequency range of the measurements and for the 0–400 Hz range the spacing was 3 cm. The acceleration signals were acquired using an HP 5420A Signal Analyzer and transferred to a PC-compatible microcomputer, via an IEEE interface. The one-third octave band averaged correlation coefficients were then estimated using equation (1).

5.2. DISCUSSION OF RESULTS: ROOF VIBRATION FIELD

In the analysis presented in references [3] and [16] it was suggested that the roof vibrational field approached that of a doubly-curved shell. This suggestion was based on the geometrical characteristics of the roof and on experimental results of correlation coefficients, that were clearly different for two perpendicular directions in a certain frequency region. The estimation of the ring frequencies of the equivalent doubly curved shell model employed was not straightforward because the roof curvature varied along the two principal directions. Inspection of the roof dynamic characteristics was employed in this estimation. The lower ring frequency was estimated to be around 100 Hz as no resonant modes were present in the measured roof frequency response functions [3, 16] below this frequency. The upper ring frequency was assumed to be around 300 Hz.

From frequency response functions measured near line D (presented in reference [16]) it was observed that no mode was excited below 150 Hz and hence, the lower ring frequency in the region where line D was placed was assumed to be 150 Hz. This was the result of a different roof curvature near line D. The experimentally estimated roof modal density was almost flat above 500 Hz and approached that of an equivalent flat plate of 0·8 mm thickness. The estimated modal density for the equivalent plate is 0·56 modes/Hz [3].

In the frequency range between the lower ring frequency, and $\sqrt{2}$ times the upper ring frequency, the bending wavenumber in a doubly curved shell depends upon the wave direction. This was the reason used in reference [3] to explain the change of the spatial correlation coefficient zero crossing and shape with the lines orientation. An expression for the dispersion relationship of a doubly curved shell is presented in Appendix C. This dispersion relationship is here employed in the estimation of the centre frequency wavenumber for different wave directions. These wavenumbers were combined with equation (30) of reference [1] and the parameters for clamped edges (equation (B4) of reference [1]). Numerical integration was then used to compute the theoretical spatial correlation coefficients on the lines lines sketched in Figure 22.

In Figures 23 and 24 results on lines A, B, C and D for 250 Hz and 315 Hz one-third octave bands are presented. As shown, the variation of the experimental spatial correlation coefficients with the lines orientation is quite clear and the theoretical results were able to represent this variation. Bearing in mind that the roof curvature varied along the two principal directions and that the edges were not clearly defined, the agreement between the

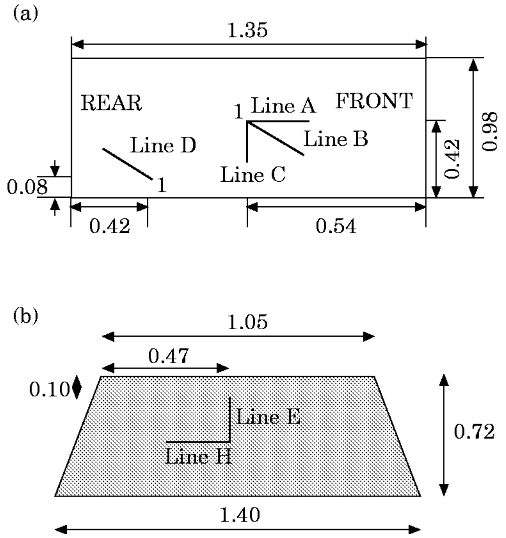

Figure 22. Position of measurement lines on (a) roof and (b) windscreen with dimensions in metres.

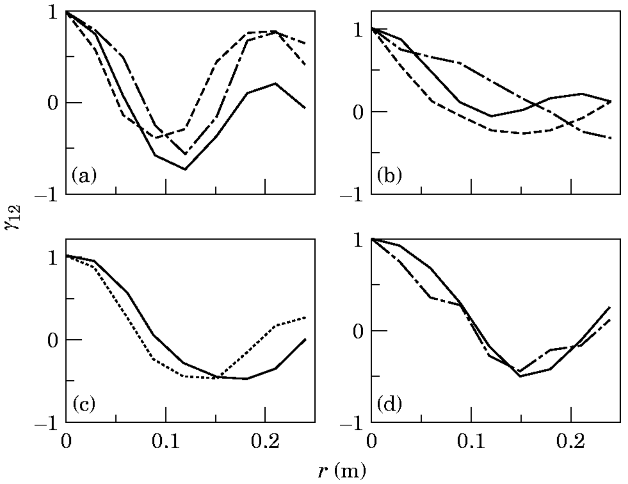

Figure 23. Roof spatial correlation coefficients, 250 Hz (one-third octave band). Key: ——, theory (equation (30), reference [1]); —·—·—, internal acoustic excitation; - - - -, external acoustic excitation; · · · ·, mechanical excitation. (a) line A; (b) line B; (c) Line C; (d) line D.

experimental and theoretical results were considered reasonable. Above the 315 Hz one-third octave band both theoretical and experimental results tended to approach the results for a diffuse bending wave field. As discussed in reference [3], only at 1000 Hz one-third octave band was the roof vibrational field considered nearly diffuse.

5.3. DISCUSSION OF RESULTS: WINDSCREEN VIBRATION FIELD

The other part of the car that could be idealised as a simple uniform structure was the windscreen. Such model is a clamped flat plate of equal windscreen area and thickness. The experimentally estimated modal density confirmed this model as a reasonable approximation for the windscreen [3]. Theoretical values of correlation coefficient were computed for points along lines E and H (illustrated at Figure 22) following this clamped

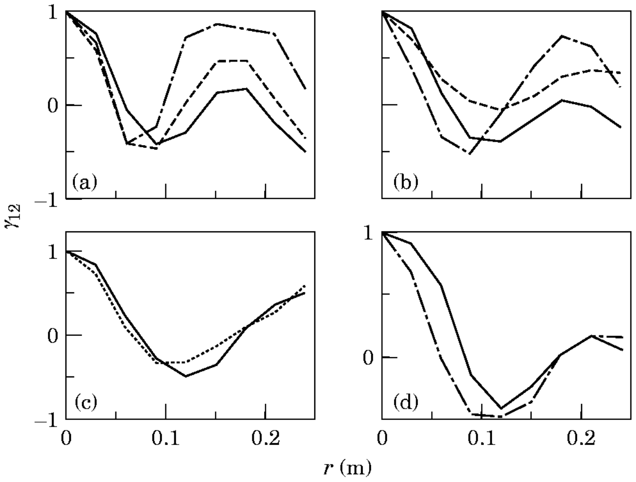

Figure 24. Roof spatial correlation coefficients, 315 Hz (one-third octave band). Key: ——, theory (equation (30), reference [1]); —·—·—, internal acoustic excitation; - - - -, external acoustic excitation; · · · ·, mechanical excitation. (a) line A; (b) line B; (c) Line C; (d) line D.

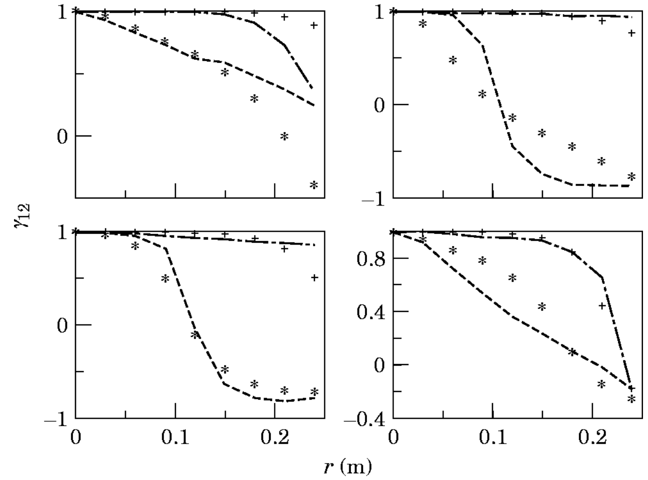

Figure 25. Spatial correlation coefficients on a passenger car windscreen. Internal acoustic excitation, one-third octave bands. Key: line E: + + +, theory; —·—·—, experiments; Line H: ***, theory; - - - -, experiments. (a) 160 Hz; (b) 200 Hz; (c) 250 Hz; (d) 315 Hz.

plate model. Typical wavelengths for the windscreen were: 0·649 m at 100 Hz, 0·458 m at 200 Hz, 0·41 m at 250 Hz and 0·365 m at 315 Hz.

Experimental results obtained at these lines are presented in Figure 25. Excitation was that set up by acoustically exciting the car interior with white noise. The fixed accelerometer for line E measurements was placed at the top of this line, close to the connection with the roof, while the fixed accelerometer for line F was placed at the junction of both lines. As shown in Figure 25, the results at both lines are quite different and in view of the relative value of the wavelength and the distance from the edges it appears that the evanescent waves generated at the top edge dominate the vibration field in the region where lines E and H were placed. The theoretical results were able to represent this influence as illustrated in Figure 25. The agreement between theoretical and experimental results were only reasonable due to non-regular geometry and low modal density ($n(f) = 0{\cdot}074$ modes/Hz) of the windscreen.

The theoretical representation suggested in part I of this work [1] appears to be a valid approximation even for practical structures like a car body shell. Some of the points raised in references [3] and [16] as reasons for the departure of the roof vibrational field from a diffuse field state, even when a large number of natural modes are assumed to be excited, have been proved to be valid. Wavenumber variation with wave propagation direction and edge boundary conditions were the points incorporated in the present theoretical model.

6. CONCLUSIONS

From the results presented in this work the following conclusions can be drawn about the theoretical model of randomly excited two-dimensional vibration fields represented in terms of spatial correlation coefficients, as presented in part I [1]:

i. For cases of low modal overlap ($M < 1$), this model is valid as a frequency-averaged estimate in bands in which at least eight to ten modes are excited at resonance. This conclusion agrees with similar one reached by Stearn [2, 12] in the analysis of diffuse bending wave fields.

ii. When the modal overlap is high ($M > 1$) this model can be used as a narrow band estimate.

iii. The validity of the present model as a broadband estimate is only limited to the increase of importance of second order terms as the bandwidth increases.

iv. For points in a region one wavelength from the edges it was found that the experimental results depart considerably from spatial correlation coefficients as given by the diffuse bending wave field assumption. The model presented in part I of this work [1] was able to reproduce with reasonable precision the distortion field created by the edges and corners.

v. Away from the edges (distance greater than at least one wavelength), the theoretical and experimental spatial correlation coefficient results approached that given by the diffuse bending wave field assumption irrespective of the boundary condition. The only exception of such agreement is for specific lines in which there is a superposition of nodal lines.

vi. When the Bolotin's dynamic edge effect parameters (Appendix B of reference [1]) are employed, the experimental results obtained on simply-supported, clamped and free plates are predicted with reasonable precision using the present model.

vii. For the case of spring supported boundaries (like stiffeners), the correlation characteristics of the vibration fields on the reflection and transmission sides are satisfactorily predicted.

viii. Despite the fact that the theoretical results were derived using the assumption of spatially uncorrelated random excitation, it was experimentally verified that they can be used as an approximation for cases of mechanically excited plates.

ix. When the theoretical results are modified in order to account for changes in the wavenumber due to curvature effects (Appendix C), the experimental results obtained on a car roof are reasonably well predicted by the proposed model.

ACKNOWLEDGMENT

The financial support of CAPES (Brazilian Government Agency for Postgraduate Education) is here acknowledged.

REFERENCES

1. M. W. Bonilha and F. J. Fahy 1998 *Journal of Sound and Vibration* **214**, 443–467. On the vibration field correlation of randomly excited flat plate structures, I: theory.
2. S. M. Stearn 1969 *Journal of Sound and Vibration* **9**, 21–27. Measurements of correlation coefficients of acceleration on a randomly excited structure.
3. M. W. Bonilha and F. J. Fahy 1994 *Applied Acoustics* **43**, 1–18. Measurements of vibration field correlation on a car body shell.
4. A. D. Pierce 1989 *Acoustics*: *An Introduction to Its Physical Principles and Applications*. New York: Acoustical Society of America.
5. R. V. Waterhouse 1955 *Journal of the Acoustical Society of America* **27**, 247–258. Interference patterns in reverberant sound fields.
6. R. V. Waterhouse and R. K. Cook 1965 *Journal of the Acoustical Society of America* **37**, 424–428. Interference patterns in reverberant sound fields II.
7. M. W. Bonilha 1996 *Ph.D. Thesis*, *University of Southampton*. A hybrid deterministic–probabilistic model for vibroacoustic studies.
8. R. D. Blevins 1979 *Formulas for Natural Frequency and Mode Shape*. New York: Van Nostrand Reinhold.
9. M. P. Norton 1989 *Fundamentals of Noise and Vibration Analysis for Engineers*. Cambridge: Cambridge University Press.
10. M. F. Ranky and B. L. Clarkson 1983 *Journal of Sound and Vibration* **89**, 309–323. Frequency average loss factors of plates and shells.

11. A. D. Mohammed 1990 *Ph.D. Thesis*, *University of Southampton*. A study of uncertainty in applications of statistical energy analysis.
12. S. M. Stearn 1970 *Ph.D. Thesis*, *University of Southampton*. Stress distributions in randomly excited structures.
13. L. Cheng and J. Nicolas 1992 *Journal of the Acoustical Society of America* **91**, 1504–1513. Radiation of sound into a cylindrical enclosure from a point-driven end plate with general boundary conditions.
14. V. V. Bolotin 1984 *Random Vibration of Elastic Systems*. The Hague: Martinus Nijhoff Publishers.
15. K. F. Graff 1975 *Wave Motion in Elastic Solids*. New York: Dover.
16. M. W. Bonilha and F. J. Fahy 1993 *ISVR Technical Report No*. 220, *University of Southampton*. Measurements of correlation coefficients of vibration on a car body shell.
17. J. S. Bendat and A. G. Piersol 1986 *Random Data*: *Analysis and Measurements Procedures*. New York: John Wiley; second edition.
18. D. E. Newland 1993 *An Introduction to Random Vibrations*, *Spectral & Wavelet Analysis*. London: Longman; third edition.
19. L. Cremer, M. Heckl and E. E. Ungar 1987 *Structure Borne Sound*: *Structural Vibration and Sound Radiation at Audio Frequencies*. Berlin: Springer Verlag; second edition.
20. R. S. Langley 1991 *Journal of Sound and Vibration* **145**, 261–277. An elastic wave technique for the free vibration analysis of plate assemblies.
21. V. V. Bolotin 1960 *Applied Mathematical Mechanics* (*PMM*) **24**, 831–843. The edge effect in the oscillations of elastic shells.
22. A. L. Gol'Denveizer 1970 *Applied Mathematical Mechanics* (*PMM*) **34**, 952–956. On the frequency distribution density of oscillations of a thin shell.

APPENDIX A: ERRORS ASSOCIATED WITH THE SPATIAL CORRELATION COEFFICIENT ESTIMATION

The variance and the confidence limits of the experimental measurements presented in this work are estimated following the procedure suggested by Bendat and Piersol [17] and Newland [18]. Random errors associated with statistical sampling considerations and bias errors associated with data acquisition errors are considered. From Bendat and Piersol [17] the normalised random error associated with the auto-spectrum estimation is

$$\epsilon_r^G = \sigma_G / m_G = 1/\sqrt{B_e T_t} \approx \frac{1}{\sqrt{n_d}}, \tag{A1}$$

where σ is the standard deviation of the measurement of average m, n_d is the number of non-overlapping averages and T_t is the total duration of the record data. The normalised bias error is a function of the resolution bandwidth, B_e, and of the system half-power bandwidth, $B_r \approx 2\zeta f_d$, where ζ is the damping ratio and f_d is the damped natural frequency. The normalised bias error for auto-spectrum measurements is given by [9]

$$\epsilon_b^G = -\tfrac{1}{3}\left(\frac{B_e}{B_r}\right)^2, \tag{A2}$$

and the normalised r.m.s. error is expected as

$$\epsilon = \sqrt{\epsilon_r^2 + \epsilon_b^2}. \tag{A3}$$

Since, in the present measurements, the bias errors associated with the auto-spectrum estimation were normally much smaller than the random errors one can say that the normalised r.m.s. error is approximately equal to the normalised random error.

Assuming the probability density function for the estimates G to be approximated by a chi-square distribution one can obtain confidence intervals for these measurements [18].

The number of degrees of freedom (κ) of the chi-square distribution is related to the standard deviation and measurement average by

$$\sqrt{2/\kappa} = \sigma/m. \tag{A4}$$

By knowing the number of degrees of freedom one can obtain confidence limits from statistical tables of percentage points of a chi-square distribution [17, 18].

The normalised random error associated with the real part of the cross-spectrum can be obtained from expression (9.25) of reference [17]. After some mathematical manipulation this gives

$$\epsilon_r = \sqrt{G_{xx}\,G_{yy} + (\mathrm{Re}\,[G_{xy}])^2 - (\mathrm{Im}\,[G_{xy}])^2}/\sqrt{2n_d}\;\mathrm{Re}\,[G_{xy}]. \tag{A5}$$

Assuming the imaginary part of the cross-spectrum, G_{xy}, to be negligible compared to the real part one can show that equation (A5) is equal to

$$\epsilon_r = (1/\sqrt{2n_d})\sqrt{(1 + \gamma_{xy}^2)/\gamma_{xy}^2}, \tag{A6}$$

where γ_{xy}^2 is the ordinary coherence function. For cases in which the coherence function is close or equal to one, the normalised random error associated with the cross-spectrum approaches the normalised random error associated with the auto-spectrum (equation (A1)).

The random error associated with the spatial correlation coefficient can be derived following the procedure outlined in section 9.2.3 of reference [17]. Assuming the imaginary part of the cross-spectral density is negligible in comparison to the real part one obtains

$$\epsilon_r^\gamma = \sigma_\gamma\,/m_\gamma \approx \sqrt{(1 - \gamma_{xy}^2)/\gamma_{xy}^2\,n_d}. \tag{A7}$$

The above expression shows that when the coherence function equals unity the random error associated with the spatial correlation coefficient is zero. Results for other values of the coherence function are shown in Table A1. The number of non-overlapping averages used in the correlation coefficient estimation was 50.

As shown, the number of degrees of freedom of the chi-square distribution were reasonably high for practical values of the coherence function. In most of the experiments performed the average value for the coherence function was in the band 1·0–0·9. In particular, when the coherence function equals 0·7 one has that the 95% confidence limits for the spatial correlation coefficient are given by

$$0{\cdot}742\gamma_{12} < m < 1{\cdot}296\gamma_{12}. \tag{A8}$$

Similarly the random errors associated with the estimation of the auto-spectrum of acceleration are defined by equation (A1). In this case, one obtains that ninety per cent of all values of the autospectrum G_{xx} will lie in the band

$$0{\cdot}779G_{xx} < m < 1{\cdot}243G_{xx}. \tag{A9}$$

TABLE A1

Random error (equation (A7)) associated with spatial correlation coefficient estimation as a function of the ordinary coherence function

γ_{xy}^2	0·9	0·7	0·5	0·3
ϵ_r^γ	0·065	0·1207	0·1732	0·2463
κ	473	137	66·7	33·0

The confidence limits presented in (A8) and (A9) show that the experimental results of spatial correlation coefficient presented in this work have low values of random error.

APPENDIX B: DERIVATION OF REFLECTION AND TRANSMISSION COEFFICIENTS FOR EDGES WITH GENERAL SPRING ATTACHMENT

As a means of deriving the reflection coefficients of edges supported by general spring elements a travelling bending wave is assumed to be incident upon a plate edge. This wave has a frequency ω and a wavenumber $k = \omega^{1/2}(m/D)^{1/4}$, where D is the flexural rigidity and m is the plate mass per unit area. The spring element provides translational, rotational and coupling resistance. The respective stiffness are k_{zz}, $k_{\theta\theta}$ and $k_{z\theta}$ (illustrated in Figure B1). The motion on both sides of the plate edge is represented in wave terms as [19, 20]

$$z_1(t) = \{A_{ref}\, e^{-ik_y y} + A_{in}\, e^{ik_y y} + A_{e_1}\, e^{-\mu_y y}\}\, e^{ik_x x}\, e^{i\omega t}, \tag{B1}$$

$$z_2(t) = \{A_t\, e^{ik_y y} + A_{e_2}\, e^{\mu_y y}\}\, e^{ik_x x}\, e^{i\omega t}, \tag{B2}$$

where A_{ref} is the modulus of the reflected wave, A_{in} represents the incident wave, A_t is the amplitude of the transmitted wave, $k_y = k \sin\theta$, $k_x = k\cos\theta$, $\mu_y = \sqrt{k^2 + k_x^2}$, A_{e1} and A_{e2} are the amplitudes of the evanescent field components on the left and right sides of the edge, respectively. The boundary conditions at $y = 0$ are

$$z_1(t) = z_2(t), \qquad \partial z_1/\partial y = \partial z_2/\partial y,$$

$$D\left[\frac{\partial^3 z_1}{\partial y^3} + (2-\nu)\frac{\partial^3 z_1}{\partial y\,\partial x^2}\right] - D\left[\frac{\partial^3 z_2}{\partial y^3} + (2-\nu)\frac{\partial^3 z_2}{\partial y\,\partial x^2}\right] = k_{zz}\, z_1 + k_{z\theta}\left(\frac{\partial z_1}{\partial y}\right),$$

$$-D\left[\frac{\partial^2 z_1}{\partial y^2} + \nu\frac{\partial^2 z_1}{\partial x^2}\right] + D\left[\frac{\partial^2 z_2}{\partial y^2} + \nu\frac{\partial^2 z_2}{\partial x^2}\right] = k_{\theta\theta}\left(\frac{\partial z_1}{\partial y}\right) + k_{z\theta}\, z_1. \tag{B3}$$

For the case in which the plate on the left side of the edge is moving, the system of equations (B3) can be solved to determine the amplitudes of the reflected, transmitted and evanescent field components. After some mathematical manipulation one can express the system of equations (B3) as

$$A_{ref} + A_{in} + A_{e1} - A_t - A_{e2} = 0, \qquad -ik_y\, A_{ref} + ik_y\, A_{in} - \mu_y\, A_{e1} - ik_y\, A_t - \mu_y\, A_{e2} = 0,$$

$$L_1\, A_{ref} + L_2\, A_{in} + L_3\, A_{e1} + L_4\, A_t + L_5\, A_{e2} = 0,$$

$$L_6\, A_{ref} + L_7\, A_{in} + L_8\, A_{e1} + L_9\, A_t + L_{10}\, A_{e2} = 0, \tag{B4}$$

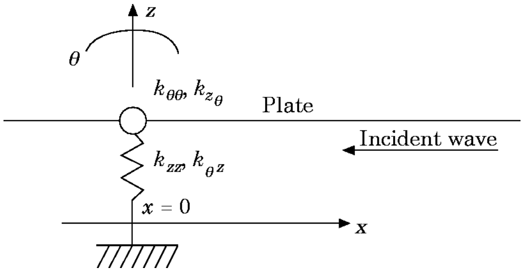

Figure B1. Elastic wave incident on a general spring attachment (reference [20]).

where

$$L_1 = \mathrm{i}Dk_y^3 - k_{zz} + \mathrm{i}k_y k_{z\theta}, \qquad L_2 = -\mathrm{i}Dk_y^3 - k_{zz} - \mathrm{i}k_y k_{z\theta}, \qquad L_3 = -D\mu_y^3 - k_{zz} + \mu_y k_{z\theta},$$

$$L_4 = \mathrm{i}Dk_y^3, \qquad L_5 = -D\mu_y^3, \qquad L_6 = Dk_y^2 - k_{z\theta} + \mathrm{i}k_y k_{\theta\theta}, \qquad L_7 = Dk_y^2 - k_{z\theta} - \mathrm{i}k_y k_{\theta\theta},$$

$$L_8 = -D\mu_y^2 - k_{z\theta} + \mu_y k_{\theta\theta}, \qquad L_9 = -Dk_y^2, \qquad L_{10} = D\mu_y^2.$$

By solving this system of equations, one obtains the amplitude of the transmitted wave as a function of the incident wave's amplitude as

$$A_t/A_{in} = T = (W_1 W_2 - W_3 W_4)/(W_5 W_4 + W_2 W_6). \tag{B5}$$

The amplitude of the evanescent field component on the left side of the spring element is given by,

$$A_{e2}/A_{in} = E_2 = [W_3 (W_5 W_4 + W_2 W_6) + W_5 (W_1 W_2 - W_3 W_4)]/W_2 (W_5 W_4 + W_2 W_6). \tag{B6}$$

The amplitude of the evanescent field component on the right side of the spring element is,

$$\frac{A_{e1}}{A_{in}} = E_1 = \frac{(L_1 - L_2)}{(L_3 - L_1)} - \frac{(L_4 + L_1)}{(L_3 - L_1)}\left[\frac{(W_1 W_2 - W_3 W_4)}{(W_5 W_4 + W_2 W_6)}\right]$$

$$-\frac{(L_5 + L_1)}{(L_3 - L_1)}\left[\frac{W_3 (W_5 W_4 + W_2 W_6) + W_5 (W_1 W_2 - W_3 W_4)}{W_2 (W_5 W_4 + W_2 W_6)}\right]. \tag{B7}$$

And finally the amplitude of the reflected wave as a function of the amplitude of the incident wave is expressed as

$$\frac{A_{ref}}{A_{in}} = R = \frac{(L_2 - L_3)}{(L_3 - L_1)} + \frac{(L_4 + L_3)}{(L_3 - L_1)}\left[\frac{(W_1 W_2 - W_3 W_4)}{(W_5 W_4 + W_2 W_6)}\right]$$

$$+\frac{(L_5 + L_3)}{(L_3 - L_1)}\left[\frac{W_3 (W_5 W_4 + W_2 W_6) + W_5 (W_1 W_2 - W_3 W_4)}{W_2 (W_5 W_4 + W_2 W_6)}\right], \tag{B8}$$

where

$$W_1 = (L_1 - L_2)(\mathrm{i}k_y - \mu_y) + (L_3 - L_1)\mathrm{i}2k_y,$$

$$W_2 = (L_6 + L_{10})(\mathrm{i}k_y - \mu_y) - (L_6 - L_8)(\mathrm{i}k_y + \mu_y),$$

$$W_3 = (L_6 - L_7)(\mathrm{i}k_y - \mu_y) - (L_6 - L_8)\mathrm{i}2k_y,$$

$$W_4 = (L_3 - L_1)(\mathrm{i}k_y + \mu_y) + (L_5 + L_1)(\mathrm{i}k_y - \mu_y),$$

$$W_5 = (L_6 - L_8)\mathrm{i}2k_y - (L_6 + L_9)(\mathrm{i}k_y - \mu_y), \qquad W_6 = (L_3 - L_1)\mathrm{i}2k_y + (L_4 + L_1)(\mathrm{i}k_y - \mu_y).$$

The above coefficients are equivalent to the reflection and transmission coefficients presented in Appendix A of reference [20]. Expressions for k_{zz}, $k_{\theta\theta}$, $k_{z\theta}$ for the case of a general stiffener are presented in Appendix B of reference [1]. The coefficients here presented can be converted in Bolotin's dynamic edge effect method parameters (as described in reference [1]) by using the following relations derived in reference [7]

$$\sin k_x \xi_x = [\tfrac{1}{2}(1 + \mathrm{Re}\,[R_L])]^{1/2}, \qquad \cos k_x \xi_x = [\tfrac{1}{2}(1 - \mathrm{Re}\,[R_L])]^{1/2},$$

$$\sin k_y \xi_y = [\tfrac{1}{2}(1 + \mathrm{Re}\,[R_B])]^{1/2}, \qquad \cos k_y \xi_y = [\tfrac{1}{2}(1 - \mathrm{Re}\,[R_B])]^{1/2} \tag{B9}$$

and

$$C_x = [\tfrac{1}{2}\,\mathrm{Re}\,[A_{e1}/A_{in}]]^{1/2} = [\tfrac{1}{2}\,\mathrm{Re}\,[|E_1|]]^{1/2}, \tag{B10}$$

where the L and B stands for the left and bottom edges. The above equations (B9) and (B10) allows the determination of the dynamic edge effect method parameters directly from the reflected and evanescent field component coefficients. Moreover, if the dynamic edge effect method is to be applied in the vicinity of a edge in which only the transmitted (A_t) and the transmitted evanescent (A_{e2}) field components exist, these equations can provide a way of estimating the dynamic edge effect parameter for the indirectly driven side of a system. In this case, the reflection wave coefficient (R) is substituted by the transmission wave coefficient (T) and the evanescent reflected field component coefficient (E_1) is substituted by the evanescent transmission field component coefficient (E_2) in equations (B9) and (B10). This is the procedure used in the estimation of the theoretical results presented in Figure 15.

APPENDIX C: DISPERSION RELATION FOR A DOUBLY CURVED THIN SHELL

An asymptotic expression for the natural frequencies of free oscillations of a doubly curved thin shell that is valid under certain conditions has been derived by Bolotin [21] using the dynamic edge effect method. This expression is [21]

$$\omega^2 = D/\rho h[(k_x^2 + k_y^2)^2 + (Eh/Dr_x^2)\,((k_x^2\,X + k_y^2)^2/(k_x^2 + k_y^2)^2)] \tag{C1}$$

where $X = r_x/r_y$, $\theta = \mathrm{arctg}\,k_y/k_x$, $D = Eh^3/(1 - \nu^2)$, ω is the frequency of the free oscillation of the shell, D is the cylindrical rigidity, ρ is the material density, h is the shell thickness, E is the Young's modulus, k_x and k_y are the wavenumbers in the x and y directions, and r_x and r_y are the principal radii of curvature of the surface. The parameter X satisfies the inequalities $-1 \leqslant X \leqslant 1$. The "plane stress" ring frequencies of the shell are defined as

$$f_x = (1/2\pi r_y)\sqrt{E/\rho}, \qquad f_y = (1/2\pi r_x)\sqrt{E/\rho}, \tag{C2}$$

where one assumes that $f_y \geqslant f_x$. Expressing the wavenumbers k_x and k_y as a function of the bending wavenumber k and angle θ one has that [22]

$$\omega^2 = D/\rho h[k^4 + (Eh/Dr_x^2)\,(X\cos^2\theta + \sin^2\theta)^2] \tag{C3}$$

where $k_x = k\cos\theta$ and $k_y = k\sin\theta$. The limits of applicability and the general behaviour of equation (C3) have been discussed by Gol'denveizer [22]. The natural frequencies of free oscillation of the shell are strongly dependent on the ring frequencies. Operating expression (C3) mathematically one obtains an asymptotic expression for the bending wavenumber.

$$k^4 = \rho h(2\pi f)^2/D - (Eh/Dr_x^2)\,(X\cos^2\theta + \sin^2\theta)^2. \tag{C4}$$

The first term on the left side of the above equation corresponds to the bending wavenumber of an equivalent flat plate while the second term is a correction due to the shell curvature. It will only have complex solutions for $f < f_x$, complex and real solutions for $f_x \leqslant f \leqslant f_y$ (curve marked 2 in Figure C1) and real solutions for $f \geqslant f_y$ (curve marked 4 in Figure C1). In the frequency region $f_x \leqslant f < f_y$, the real solutions are situated in a curve delimited by the angles 0 and θ_0, where θ_0 is given by

$$\theta_0 = \tfrac{1}{2}\cos^{-1}([2f/f_y - (X + 1)]/(X - 1)). \tag{C5}$$

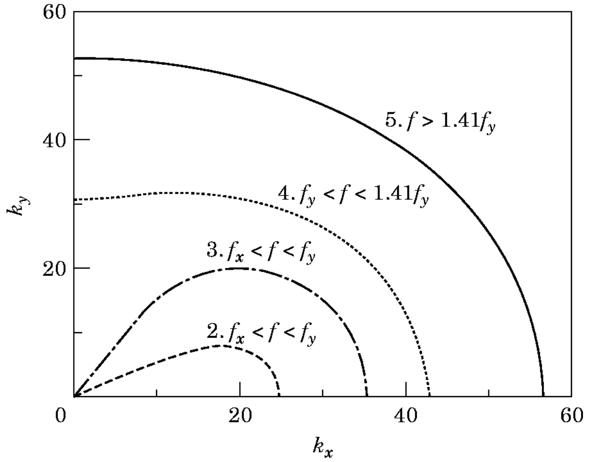

Figure C1. Dispersion relations for a doubly curved shell of positive curvature ($X > 0$) and ring frequencies $f_x = 100$ Hz and $f_y = 300$ Hz. Key to frequency of oscillation: 2, $f = 150$ Hz; 3, $f = 250$ Hz; 4, $f = 350$ Hz; 5, $f = 600$ Hz.

In the frequency $\sqrt{2}$ times the upper ring frequency the shell bending wavenumber approaches that of the equivalent flat plate (curve marked 5 in Figure C1).

Equation (C4) was used to estimate the bending wavenumber of the passenger car roof in the theoretical results presented in section 5. In this case, for frequencies situated between the two ring frequencies, the integration in wavenumber space used in the correlation coefficient estimation was performed between 0 and θ_0, where θ_0 is given by equation (C5). Below the lower ring frequency no integration was performed and the correlation coefficient was assumed to approach unity. Above the upper ring frequency the usual limits 0 and $\pi/2$ apply. This procedure can be applied in the estimation of spatial correlation coefficients for all curved shells. The results presented in section 5 show that a reasonable approximation of the variation of the spatial correlation coefficient results due to the lines orientation can be obtained when equation (C4) is employed.